

Value of nonstationary wavelet spectral balancing in mapping a faulted fluvial system, Bohai Gulf, China

Huailai Zhou¹, Yuanjun Wang², Tengfei Lin³, Fangyu Li³, and Kurt J. Marfurt³

Abstract

Seismic data with enhanced resolution allow interpreters to effectively delineate and interpret architectural components of stratigraphically thin geologic features. We used a recently developed time-frequency domain deconvolution method to spectrally balance nonstationary seismic data. The method was based on polynomial fitting of seismic wavelet magnitude spectra. The deconvolution increased the spectral bandwidth but did not amplify random noise. We compared our new spectral modeling algorithm with existing time-variant spectral-whitening and inverse Q -filtering algorithms using a 3D offshore survey acquired over Bohai Gulf, China. We mapped these improvements spatially using a suite of 3D volumetric coherence, energy, curvature, and frequency attributes. The resulting images displayed improved lateral resolution of channel edges and fault edges with few, if any artifacts associated with amplification of random noise.

Introduction

Enhancing the resolution of surface seismic data is key to improving images of thin geologic features common to fluvial systems. High-resolution facilitates horizon interpretation, highlights sequence boundaries, and sharpens attribute images.

Chopra and Marfurt (2007) find that seismic data with limited resolution gives rise to lower resolution seismic attribute and inversion volumes due to narrow frequency bandwidth, thereby hindering the delineation of subtle reservoir features. Conversely, seismic attributes computed on seismic reflection data having enhanced resolution can facilitate quantitative and qualitative interpretation and reveal the spatial distribution of structural and stratigraphic features. In fact, the quality and reliability of reservoir characterization based on seismic attributes, such as coherence, curvature, dip-azimuth, and impedance inversion depend directly on the seismic resolution.

Algorithms to improve seismic resolution fall into two broad categories: time-variant spectral balancing (deconvolution) and inverse Q -filtering. The goal of deconvolution is to compress the seismic wavelet and attenuate reverberations as well as short-period multiples by estimating the earth's reflectivity (Rosa and Ulrych, 1991; Ziolkowski, 1991; Margrave and Lamoureaux, 2001;

Yilmaz, 2001; Margrave et al., 2011; Wang et al., 2013). Chopra et al. (2006) propose an alternative "thin-bed spectral inversion" that removes the time-variant wavelet from the seismic data using a matching-pursuit variant of sparse spike inversion of time-frequency spectral components. The goal of inverse Q -filtering is to compensate for nonstationary attenuation (Futterman, 1962; Kjartansson, 1979; Hale, 1982; Hargreaves and Calvert, 1991; Hargreaves, 1992; Zhang et al., 2007; Wang, 2010). In practice, it is difficult to estimate a stable and accurate Q -model that represents intrinsic and geometric attenuation as waves propagate.

Time-variant deconvolution and inverse Q -filtering algorithms operate implicitly or explicitly in the time-frequency domain. Hence, time-frequency transform methods, which decompose nonstationary seismic signal into a series of nonstationary time-frequency atoms, form the basis of spectral resolution enhancement. Current time-frequency transforms include the Gabor transform (Gabor, 1946), the short time Fourier transform (STFT) (Partyka et al., 1999; Marfurt and Kirlin, 2001), the continuous wavelet transform (CWT) (Rioul and Vetterli, 1991; Matos et al., 2009), empirical mode decomposition (EMD) (Huang et al., 1998), the seislet transform (Fomel and Liu, 2010), S-transform (Stockwell et al., 1996), the generalized S-transform (GST) (McFadden et al., 1999; Gao et al., 2003; Pinnegar

¹Chengdu University of Technology, State Key Laboratory of Oil and Gas Reservoir Geology and Exploitation, Key Lab of Earth Exploration and Information Techniques of Ministry of Education, College of Geophysics, Chengdu, Sichuan, China and The University of Oklahoma, ConocoPhillips School of Geology and Geophysics, Norman, Oklahoma, USA. E-mail: zhouhuailai06@cdut.cn.

²Chengdu University of Technology, College of Geophysics, Chengdu, Sichuan, China. E-mail: wyj_cdut@163.com.

³The University of Oklahoma, ConocoPhillips School of Geology and Geophysics, Norman, Oklahoma, USA. E-mail: tengfei.lin@ou.edu; fangyu.li@ou.edu; kmarfurt@ou.edu.

Manuscript received by the Editor 29 June 2014; revised manuscript received 7 September 2014; published online 11 March 2015. This paper appears in *Interpretation*, Vol. 3, No. 3 (August 2015); p. SS1–SS13, 15 FIGS.

<http://dx.doi.org/10.1190/INT-2014-0128.1>. © 2015 Society of Exploration Geophysicists and American Association of Petroleum Geologists. All rights reserved.

and Mansinha, 2003), matching pursuit related methods (Liu and Marfurt, 2007; Wang, 2007, 2010), and a local attribute using an iterative inversion framework based on regularized nonstationary regression (Fomel, 2007, 2009; Liu et al., 2011). In this paper, we compute time-frequency spectra using a GST due to its adjustable time-frequency characteristics and easy implementation. We then model these spectra with a series of wavelet spectra parameterized by low-order polynomials and spectrally balance these wavelets to obtain high time-frequency resolution seismic traces.

We begin our discussions with a review of time-variant spectral balancing and inverse Q -filtering methods. We then review key components of our time-frequency spectral-modeling algorithm. Next, we apply these three methods to a 3D offshore seismic survey acquired over the Bohai Gulf, China, and compare the results to each other and to the original data. We validate the improvement provided by the NPF algorithm by correlating synthetic seismograms from a well log in the survey. Finally, we use coherence, curvature, and mean frequency attributes to quantify the improvement in delineating lateral extent and vertical resolution of a faulted fluvial system.

Methodology

Several methods have been applied to expand the frequency bandwidth of nonstationary seismic data to compensate for attenuation. Two of the more important techniques are time-variant spectral balancing (deconvolution) and inverse Q -filtering.

Time-variant spectral balancing

Time-variant spectral whitening (TVSW) (Yilmaz, 2001) is a common method to broaden the frequency bandwidth of the seismic signal and deal with attenuation. More recently, spectral whitening may be modified to become spectral “bluing” (Neep, 2007) giving rise to the term *spectral balancing* to obtain any desired objective spectrum. TVSW divides the input seismic trace into multiple overlapping windows. Within each window, TVSW computes a suite of band-pass-filtered versions of the data (not unlike an S-transform). The envelope of each band-pass-filtered component provides a means to estimate the spectral decay rate. Next, one computes the inverse of (or otherwise compensates for) this decay rate to obtain a spectrally balanced signal within each analysis window. Finally, the output trace is constructed by blending the windows together (van der Baan, 2008). In most implementations, the window length is determined by the user rather than by the data, such that an improper choice of the window length may give rise to unsatisfactory results. In addition, high-frequency noise may be erroneously amplified that may negatively impact subsequent interpretation. More modern spectral-balancing implementations minimize the size of the vertical analysis window and obtain accurate statistics through the use of time-variant spectra of

adjacent traces, or even of the entire survey (e.g., Marfurt and Matos, 2014).

Inverse Q -filtering

Loss of higher frequencies caused by intrinsic attenuation in rocks gives rise to wavelet nonstationary behavior, such that the wavelet shape changes with time (Yilmaz, 2001). Seismic attenuation is usually described by a dimensionless quality factor Q , which is defined by the ratio of the mean-stored energy to the energy loss within a single cycle (Kjartansson, 1979). Although the previously described time-variant spectral balancing uses simple statistics (curve fitting) to estimate the attenuation, inverse Q -filtering uses fits — a deterministic spectral attenuation model to the time-varying spectral components. This model (estimate of Q) can then be used to not only boost the amplitude of the higher frequency components, but also it can compensate for the corresponding dispersion effects by rotating the phase components of seismic data (Chopra, 2011). Inverse Q -filtering works well when based on VSP measurements (Chopra et al., 2003) or on a large number of carefully constructed synthetics (Taner and Treitel, 2003). However, accurate estimation of Q directly from surface seismic data has proven to be a challenging problem.

Time-frequency domain deconvolution based on nonstationary wavelet spectra modeling

We propose a new enhanced-resolution method in time-frequency domain, which contains three steps as follows.

Step 1: Spectral decomposition of nonstationary seismic data

Time-frequency analysis provides a means to characterize the nonstationarity seismic signals. Here, we use the GST to do spectral decomposition because of its high time-frequency resolution, which is defined as

$$\hat{x}(\tau, f)_{\text{GST}} = \int_{-\infty}^{+\infty} x(t) \frac{|f|^r}{\sqrt{2\pi\sigma''}} e^{\frac{(\tau-t)^2 |f|^{2r}}{2\sigma''^2}} e^{-i2\pi f t} dt, \quad (1)$$

where $x(t)$ is the original seismic signal, τ is the time-shift parameter, and $\hat{x}(\tau, f)_{\text{GST}}$ is a 2D time-frequency variable with regard to f and τ , whereas σ'' and r are adjustable parameters that define the trade-off between temporal and spectral resolution. Testing alternative parameters on our data shows optimal time-frequency resolution for values of $\sigma'' = 1.2$ and $r = 0.8$. Examining equation 1, we see that the Gabor transform (Gabor, 1946) is a special case of the GST where $r = 0$. Similarly, one obtains the S-transform (Stockwell et al., 1996) by setting $\sigma'' = 1$ and $r = 1$.

Step 2: Spectral modeling using nonstationary polynomial fitting

Based on the assumption of statistically white reflectivity, Rosa and Ulrych (1991) model the magnitude spectra of the time-varying seismic wavelets, from a seismic amplitude trace using a smooth polynomial

in the time-frequency domain (or generalized S-domain) as

$$W_a(\tau, f_m) = |f_m|^k \exp\left(\sum_{n=0}^N a_n(\tau) f_m^n\right), \quad (2)$$

where $W_a(\tau, f_m)$ denotes a smooth amplitude spectrum of a time-varying wavelet, $a_n(\tau)$ is the n th polynomial coefficient independent on frequency at time τ , N is the lower polynomial order, and f_m is the m th frequency. Rosa and Ulrych (1991) use equation 2 to model the amplitude spectrum of a wavelet. In our implementation, the polynomial coefficients vary with time and frequency, providing a means to represent nonstationarity of seismic data more precisely than the original temporally variant fitting method. Specifically, we redefine equation 2 to obtain

$$\hat{W}_a(\tau, f_m) = |f_m|^k \exp\left(\sum_{n=0}^N a_n(\tau, f_m) f_m^n\right). \quad (3)$$

Then, we estimate the polynomial coefficients by solving the following least-squares problem:

$$\min_{a_n(\tau, f_m)} \sum_{m=1}^M \varepsilon_m^2 = \sum_{m=1}^M \left\| \ln A(\tau, f_m) - k \ln |f_m| - \left(\sum_{n=0}^N a_n(\tau, f_m) f_m^n \right) \right\|_2^2 + R[a_n(\tau, f_m)], \quad (4)$$

where $\|\cdot\|_2^2$ denotes the squared L_2 norm of a function, $A(\tau, f_m)$ denotes the time-frequency amplitude spectra of seismic trace, $a_n(\tau, f_m)$ expresses the polynomial coefficients varying with time and frequency, R denotes a regularization operator, and ε_m is the misfit error to be minimized. Here, we use “shaping regularization” (Fomel, 2007), which is integrated in a conjugate-gradient algorithm for iterative least-squares estimation and adopt the Gaussian smoothing operator with an adjustable radius to control the smoothness of the coefficients $a_n(\tau, f_m)$.

Note that the time-frequency amplitude spectra $\hat{W}_a(\tau, f_m)$ of a wavelet can be estimated by iterating the procedure of equations 3 and 4 over all the frequencies at every time sample τ . Once we obtain the nonstationary polynomial coefficients $a_n(\tau, f_m)$, we can model the wavelet spectra using the equation 3.

Step 3: Deconvolution in the time-frequency domain

We spectrally balance, or deconvolve, the seismic data by the time-frequency spectra of the seismic trace by the time-frequency spectra of the estimated seismic wavelet (equation 3) to estimate the spectrally balanced time-frequency spectra of the reflectivity. We then apply the inverse GST to obtain a spectrally balanced estimate of reflectivity in the time domain.

The noise-free synthetic example shown in Figure 1 provides a quantitative comparison of the three-candi-

date spectral balancing algorithms. Figure 1a shows a suite of random spikes, representing the ideal reflectivity. Figure 1b shows the corresponding attenuation-free synthetic obtained by convolving the reflectivity in Figure 1a with a 40-Hz Ricker wavelet. Figure 1c shows the same trace that has undergone attenuation with a quality factor $Q = 45$. Application of TVSW, inverse Q -filtering, and the NPF algorithm to Figure 1c, produces the enhanced-resolution results shown in Figure 1d–1f. Note that all three algorithms provide comparable improvements in resolution of the area within the black dashed-line box. In contrast, comparison of the results within the dashed-line ovals with the actual reflectivity clearly shows that the NPF method (Figure 1f) provides the best enhancement of resolution. Furthermore, examination of the results within the solid line rectangles of Figure 1 indicates that the noise produced by the NPF method is less than those of other two methods.

Application

The Bohai Gulf consists of a thick succession of fluvial-deltaic systems. Though many of these channels are filled with sand and form excellent reservoirs, some are filled with shale and form baffles. The key to successful development is to laterally delineate such channels and to determine whether stacked channels are either vertically separated (forming separate reservoir compartments) or whether younger channels have incised older ones (potentially forming a single reservoir compartment). Our goal is to evaluate the effectiveness time-variant spectra whitening (TVSW), inverse Q -filtering, and our new NPF spectral modeling algorithm as resolution enhancement tools. We quantify such improvements by examining key vertical slices through the seismic amplitude volumes as well as time slices through the corresponding coherence, curvature, and frequency attribute volumes.

Improvements in resolution seen on seismic amplitude volumes

In Figure 2, we show a comparison of vertical sections through the seismic amplitude data before and after the application of TVSW, inverse Q -filtering, and the proposed NPF spectral modeling method. TVSW and inverse Q -filtering (Figure 2b and 2c) provide improvements in resolution compared with original section in Figure 2a. However, examining the data within the black dashed boxes, it is clear that the NPF results shown in Figure 2d obtained by the NPF provide more reflection detail and better delineate the faults highlighted by the oblique dashed lines. In the areas indicated by the black arrows, note that the thin beds clearly resolved in Figure 2d are poorly resolved in Figure 2b and 2c.

Well logs provide ground truth, though our normal incident synthetics (which lack S-wave sonic logs) do not account for AVO effects. In Figure 3, we show a zoomed window of the data corresponding to the window within the dashed-line boxes of Figure 2. Synthetic

traces produced by convolving Ricker wavelets with reflectivity derived from well logs are inserted within each window. The correlation of the well log synthetic with the original data (Figure 3a) is 0.67, for TVSW (Fig-

ure 3b) is 0.76, for inverse Q -filtering (Figure 3c) is 0.77, and for the proposed NPF spectral modeling algorithm (Figure 3d) is 0.80. Such values indicate that the improved seismic data using the NPF method are real.

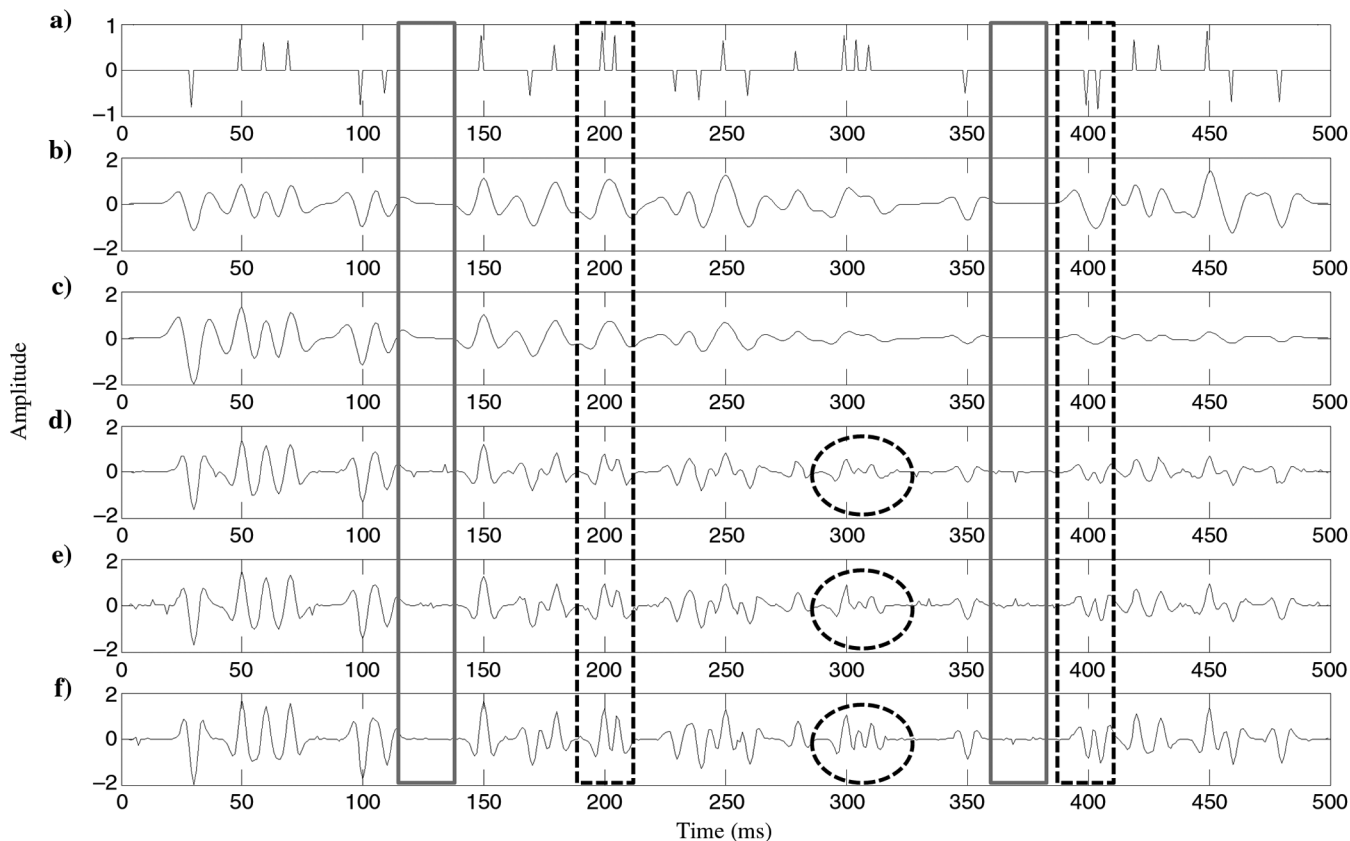
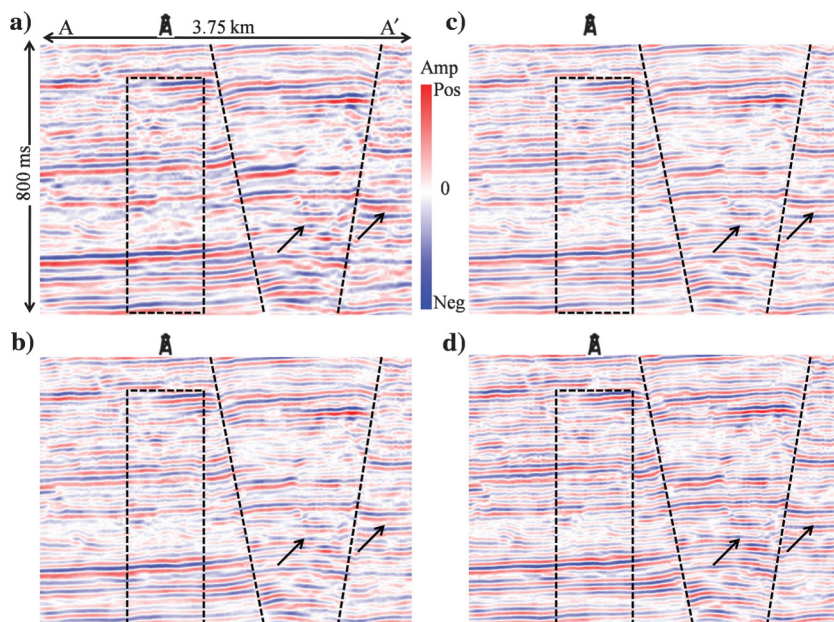


Figure 1. A noise-free synthetic seismic trace example. (a) The reflectivity. (b) The synthetic seismic trace without attenuation. (c) The synthetic seismic trace with attenuation created by $Q = 50$. Panels (d-f) show the improved resolution results applied by time-variant spectra whitening (TVSW), inverse Q -filtering, and the proposed spectral modeling method. The black dotted-line boxes and ovals denote the comparing areas. Notice that the best enhancement of seismic resolution is in Figure 1f.

Figure 2. Vertical slices along line AA' through the (a) original seismic amplitude volume and through volumes after spectral balancing using (b) after TVSW, (c) inverse Q -filtering, and (d) the proposed spectral modeling method. The oblique dashed-lines indicate the location of faults. Black arrows and dashed-line boxes indicate areas of improved vertical resolution, with the clearest identification of thin beds seen in Figure 2d. The location of line AA' is shown on subsequent time slices.



Note that the adjacent events indicated by the green arrow are resolved in Figure 3d but cannot be clearly separated in Figure 3a–3c.

Figure 4 shows corresponding time slices at $t = 510$ ms through the same volumes shown in Figure 1. Note that little random noise appears in any of the spectrally balanced time slices. Also, note that some of the channels seen in Figure 4a no longer appear in the spectrally balanced images. This “loss of geology” is common on spectrally balanced images. A given low-resolution channel seen in Figure 4a that lies above or below the target time slice will no longer be seen after spectral balancing, but rather it will be more tightly concentrated about the shallower or deeper time level where it actually occurs. This reduction in vertical smearing will carry through in subsequent attribute slices and is well documented in a recent paper by Leppard et al. (2010). Figure 5 shows average amplitude spectra for the original and three enhanced-resolution data. As expected from our previous inspection of Figure 2, the average spectrum of the section applied our proposed nonstationary polynomial fitting (NPF) deconvolution method denoted by the red solid curve is broader than those of TVSW deconvolution (green solid curve) and inverse- Q -filtering data (blue solid curve) and broader still than the original data (black solid curve). Moreover, as observed in Figure 5, the dominant frequency of the result using our NPF method is greater than the other three.

Local weighted averaging of instantaneous seismic attributes improves their interpretability by removing spikes and reducing rapid and confusing variations (Barnes, 2000). We calculate the average weighted frequency shown in Figure 6 for the corresponding section of Figure 2 to evaluate the influence of the improved resolution on the frequency components, which is performed through weighting the value of the instantaneous frequency by the instantaneous envelope and averaging over a short time window. The NPF method shows a higher weighted average frequency (Figure 6d) than the other methods, particularly around the well indicated by the black dashed-line boxes. Note the decrease in the average weighted frequency near the faults described by the oblique dashed-lines are due to either anomalous attenuation or alternatively, laterally smeared images and loss of high frequency due to an inaccurate migration velocity model.

The amplitude time slices shown in Figure 4b–4d are comparable. To determine which is “best,” we compute a suite

of attributes commonly used to map channels and faults.

Fault detection and channel delineation

Chopra and Marfurt (2007) argue that the quality of seismic data directly influences the quality of subsequent structural attributes results such as coherence, curvature, and other attributes, which can aid interpreters by enhancing subtle structural and stratigraphic features such as fault, channel, fracture, fold, and so on. To evaluate the impact of enhanced-resolution processing on coherence, in Figure 7, we display a comparison of time slices through coherence volumes computed from the original seismic data (Figure 7a) as well as from resolution-enhanced data obtained using TVSW (Figure 7b), inverse Q -filtering (Figure 7c), and the proposed NPF method (Figure 7d). Because the data have a 50-Hz component, all computations used a five-trace, ± 10 -ms analysis window. In general, coherence images from low-frequency data mix vertical stratigraphy, giving rise to the washed-out, more coherent image seen in Figure 7a, in which red arrows indicate poorly focused

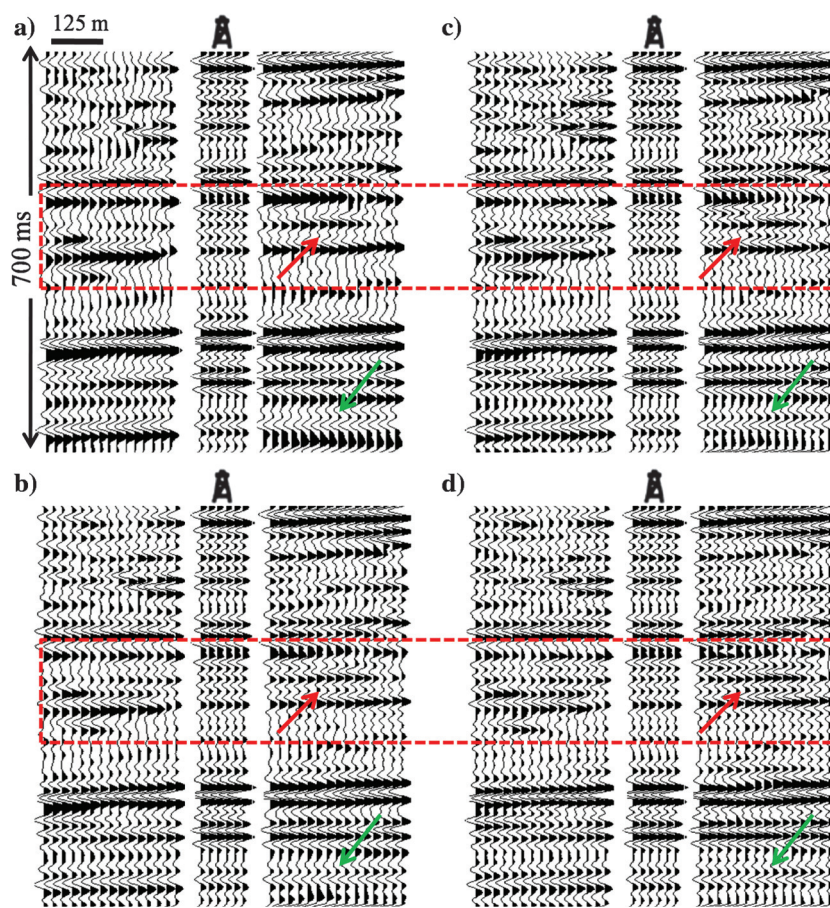


Figure 3. The zoomed view of the black dashed-line rectangle zone in Figure 2. (a) Original field seismic data. Panels (b–d), respectively, denote the results using TVSW, inverse Q -filtering, and the proposed spectral-modeling method. The synthetic obtained by convolving the Ricker wavelet with reflectivity derived from well logs is inserted in (a–d). The correlation coefficients between the synthetic and the well-side traces in (a–d) are 0.67, 0.76, 0.77, and 0.80, respectively.

Figure 4. Time slices at $t = 510$ ms through the (a) original seismic amplitude volume and through volumes after spectral balancing using (b) TVSW, (c) inverse Q -filtering, and (d) the proposed spectral-modeling method. Note that none of the spectrally balanced time slices (b-d) are contaminated by noise. Because channels may cut above or below this time slice, direct comparisons of Figure (b-d) with (a) can be misleading, with “more geology” in (a) due to adjacent channels in leaking into the time slice shown on this image.

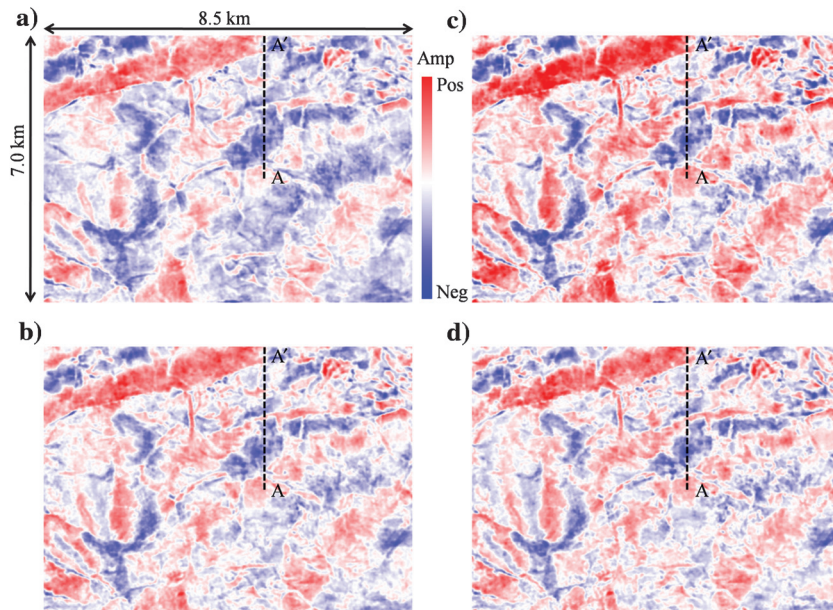


Figure 5. Comparison of average amplitude spectra of four images shown in Figure 2 for the original data (black solid curve), data after TVSW deconvolution (green solid curve), data after inverse- Q -filtering (blue solid curve) and data after the proposed method (red solid curve). Note that the dominant frequency is higher and bandwidth broader for the seismic section processed with proposed method compared to the original, TVSW deconvolution, and inverse- Q -filtering data.

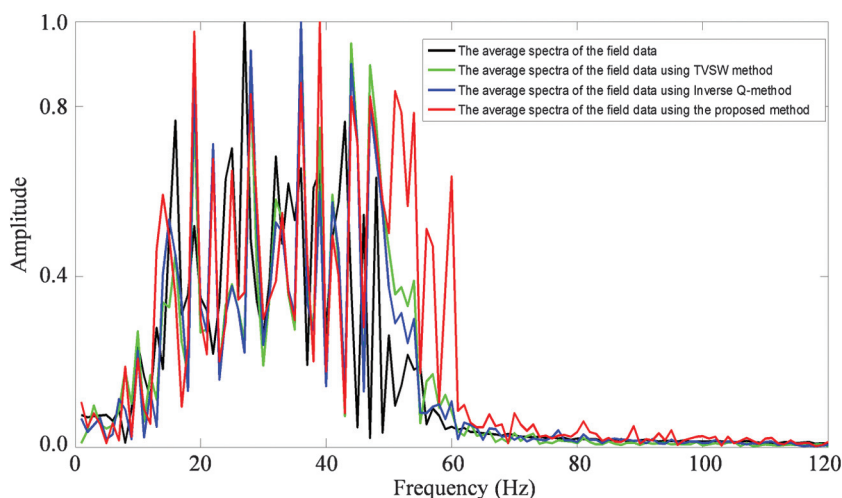
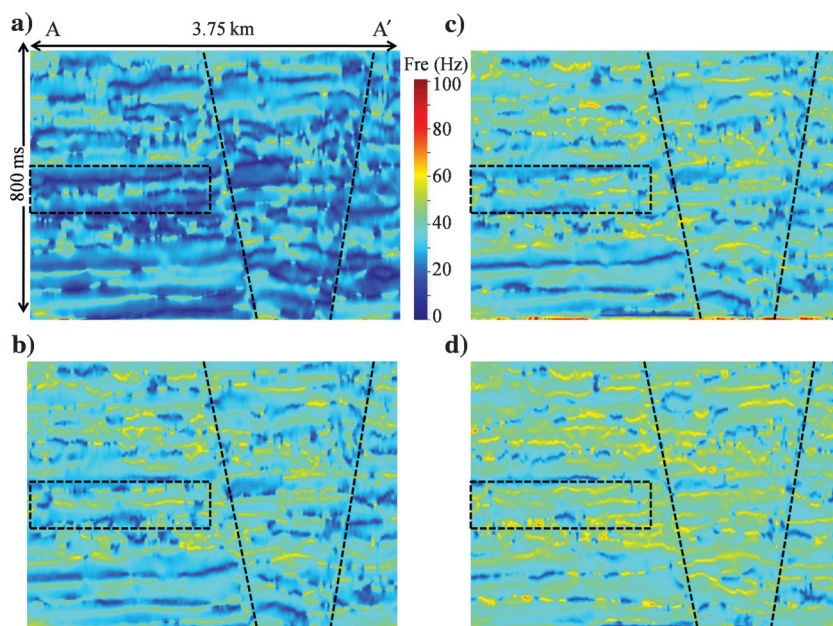


Figure 6. Vertical slices along line AA' through average weighted frequency volumes computed from the seismic amplitude volumes shown in Figures 2 and 4: (a) Original seismic amplitude and spectrally balanced volumes using (b) TVSW, (c) inverse Q -filtering, and (d) the proposed spectral modeling method. The oblique dashed line indicates the location of faults. Note that the black dashed-line boxes indicate the comparing areas of average weighted frequency components on the vertical section.



faults and green arrows indicate less poorly defined channel edges. Notice that time slices extracted from the coherence volumes run on frequency-improved data show significantly increased identification of faults discontinuity and clear delineation of channel features in Figure 7b–7d, with the highest lateral resolution and clearest delineation of major faults and channels observed from coherence in Figure 7d.

Geometric attributes often allow us to map faults on time-slice faults that may not readily seen on conventional amplitude slices (Chopra and Marfurt, 2007). Spectral components are also routinely used to map faults and channels. In Figure 8a and 8b, we show time slices through the peak frequency corendered with peak magnitude volumes and coherence computed from the original and NPF-filtered data corendered using a hue-lightness-saturation (HLS) color model. Note that the major faults on Figure 8b are clearer and the peak frequency is higher than those on Figure 8a.

In addition, we calculate multiple attributes run on the NPF enhanced-resolution data to comprehensively delineate the faults and channels. Note that all the following attribute figures in this paper are obtained from attribute volumes computed on enhanced-resolution

data using the proposed method without specific declaration. In Figure 9a, it is difficult for us to see obvious trending faults from the amplitude slice, and, needless to say, identifying the edge of channels. The corresponding coherence slice in Figure 9b (the same as Figure 7d) not only shows clear faults but also the distribution of channels indicated as the red dotted line. In Figure 9c, the instantaneous phase slice also shows faults, channels, and lateral stratigraphic changes. To clearly delineate the faults and channels, we overlay the coherence, instantaneous slices on the corresponding amplitude slice displayed in Figure 9d to help us understand the seismic expressions of the structural and stratigraphic features, and it can also reveal the corresponding relationship between seismic attributes and amplitude when delineating the same geologic phenomenon.

Next, we choose a representative seismic line perpendicular to faults of interest indicated by the dashed line BB' in Figure 9a–9c and we display the corresponding vertical slices including seismic amplitude (Figure 10a), the corresponding instantaneous phase (Figure 10b), and coherence (Figure 10c). Figure 10 reveals two main faults and some subtle faults between layers indicated by a white dotted line as we expect.

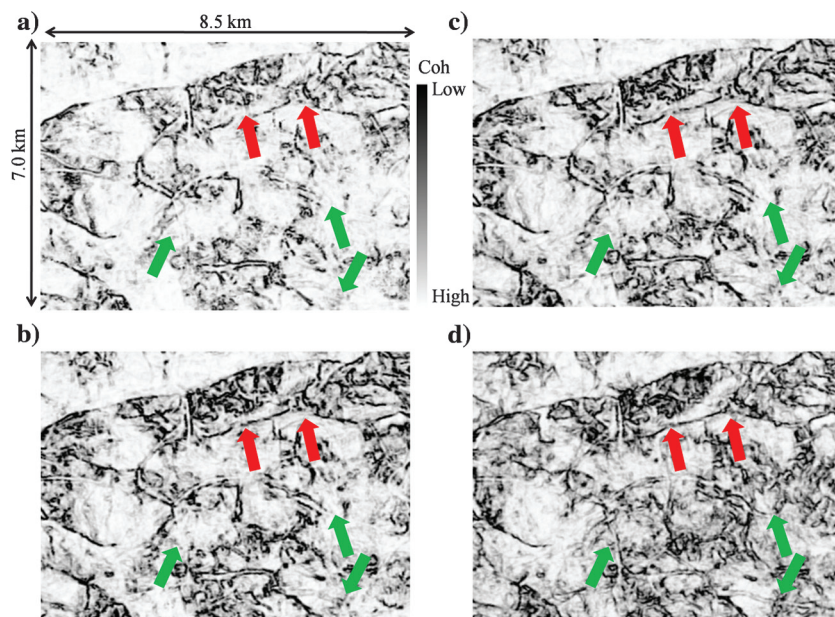


Figure 7. Time slices at $t = 510$ ms through coherence volumes computed from the seismic amplitude volumes shown in Figures 2 and 4: (a) Original seismic amplitude and spectrally balanced volumes using (b) TVSW, (c) inverse Q -filtering, and (d) the proposed spectral modeling. Note that the time slices from the coherence volumes show clearer fault features described by red arrows and more obvious channels illustrated by blue arrows in Figure 7d.

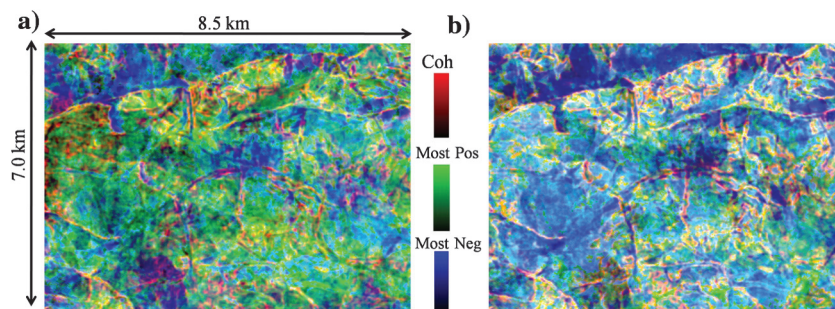


Figure 8. Time slices at $t = 510$ ms through composite volumes of peak amplitude, peak frequency, and coherence computed on (a) the original field data and (b) the enhanced-resolution data. Note that the highest lateral resolution of faults and channels is in the Figure 8b.

The most-positive and most-negative curvatures are the most unambiguous of the curvature images in highlighting faults, folds, and the edge of the channel (Chopra and Marfurt, 2007). In Figure 11, we show a comparison of time slices at $t = 510$ ms through long-wavelength and short-wavelength most-positive curvature volumes computed from the data before and after enhancing resolution to illustrate the impact of seismic resolution on the curvature attributes. Figure 11a and 11b, respectively, shows the long-wavelength and short-wavelength most-positive curvature derived from the original data volumes. As observed from the comparing points denoted by green arrows, the long-wavelength (Figure 11c), and short-wavelength (Figure 11d) most-

positive curvature computed from the enhanced-resolution data volumes demonstrate that the lateral resolution is slightly strengthened compared with the results of Figure 11a and 11b. By contrasting, we also find that the long-wavelength curvature shown in Figure 11a and 11c has an obvious advantage in delineating the lineament of faults and channels. However, the short-wavelength curvature can provide abundant, detailed information, which helps to reveal the buried geologic features as shown in Figure 11b and 11d.

To further clarify the seismic attributes characterization of faults and channels, Figure 12c demonstrates an overlay of instantaneous envelope displayed in Figure 12a and coherence attribute shown in Figure 12b.

Figure 9. Time slices at $t = 510$ ms through (a) seismic amplitude, (b) coherence, and (c) instantaneous phase volumes computed using the proposed spectral-modeling method. (d) Color stack all three attributes. The vertical dashed-line BB' indicates the location of Figure 10a and 10c on the time slice. Note that the overlay facilitates marking the extent and trend of the channel features described by red dotted line and aids in delineating the faults.

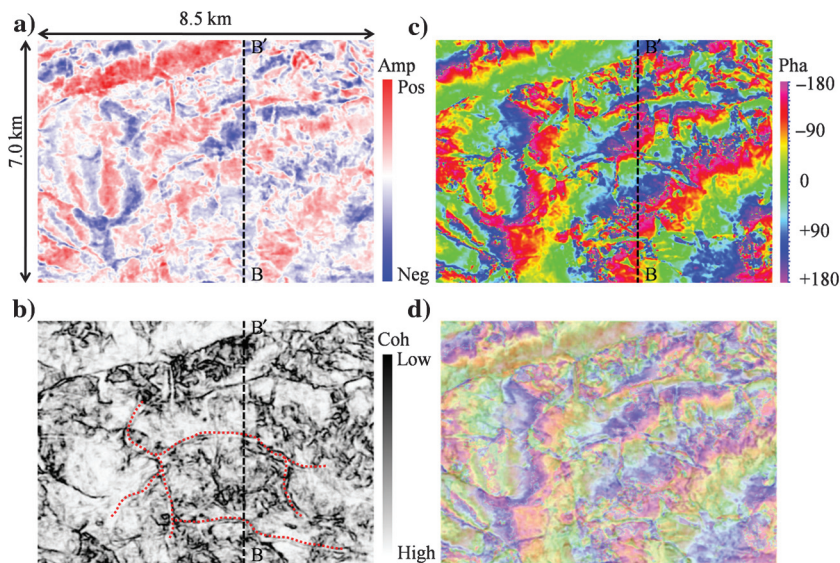
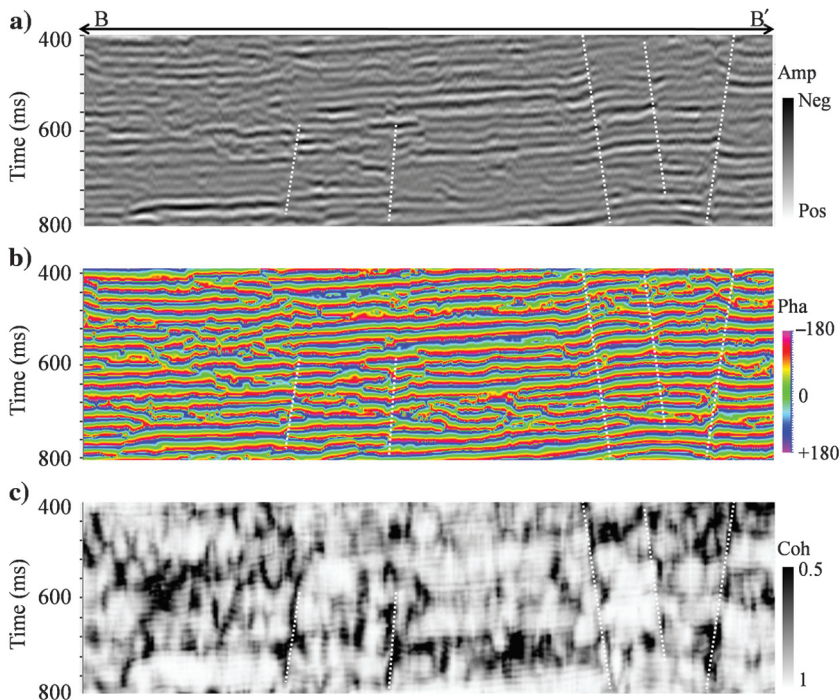


Figure 10. A vertical slice BB' through (a) seismic data, (b) instantaneous phase, and (c) coherence volumes corresponding to Figure 9a–9c. The white dotted lines indicate the faults.



Similarly, we overlay curvature attribute shown in Figure 11c and coherence attribute displayed in Figure 12b to get Figure 12d. The overlays shown in Figure 12c and 12d reveal that the lineaments in red seen on the most-positive curvature will correlate with the upthrown signatures that may be corresponding to the sharp variance area of instantaneous envelope or low coherence and obviously indicate the location and trend of faults and channels.

In Figure 13, we depict a suite of time slices through the long-wavelength (Figure 13a) and short-wavelength (Figure 13b) most-negative curvature volumes computed from the seismic data, and the long-wavelength (Figure 13c) and short-wavelength (Figure 13d) most-negative curvature volumes run on the enhanced-resolution data. Compared with the most-positive curvature displayed in Figure 11, subtle channels described as

green arrows are clearly shown in Figure 13, with the highest lateral resolution in Figure 13c and 13d. In this case, note that delineation of faults and channels is not specifically obvious such as that observed on the coherence attribute shown in Figure 12b, which may be explained by the fact the curvature attribute is more sensitive to the structural variances than coherence.

Similar to Figure 12, for the convenience of comparison, in Figure 14, we display the time slices of the most-positive curvature (Figure 14a, same as Figure 11c), most-negative curvature (Figure 14c), coherence (Figure 14b, same as 12b), and an overlay (Figure 14d) of three attributes stated above. In Figure 14d, we can observe the lineaments in blue seen on the most-negative curvature slice will correlate with the downthrown signatures. Because the positive curvature tightly correlates to a channel seen on coherence, it is an indicator that it has

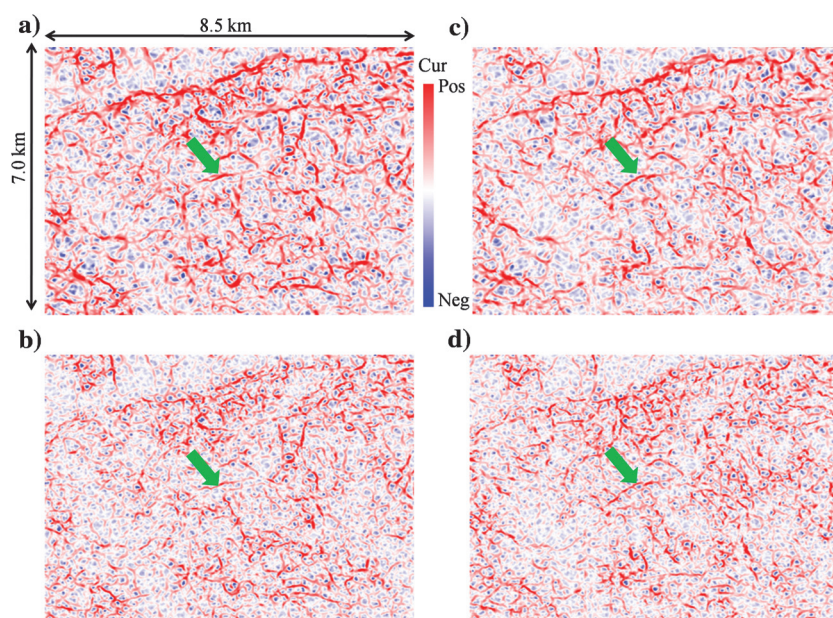


Figure 11. A time slice at $t = 510$ ms through (a) most-positive curvature (long-wavelength) and (b) most-positive curvature (short-wavelength) volumes run on input seismic data, (c) most-positive curvature (long-wavelength), and (d) most-positive curvature (short-wavelength) volumes run on seismic data with enhanced resolution. Note that the lateral resolution denoted by the green arrows is slightly strengthened in Figure 11c and 11d.

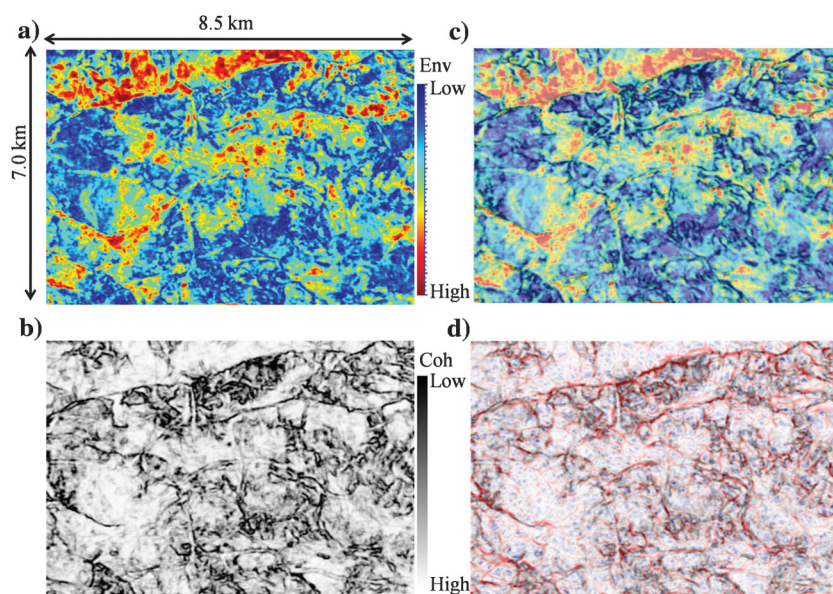


Figure 12. A time slice at $t = 510$ ms through the (a) instantaneous envelope data volume, (b) coherence volume, (c) instantaneous envelope overlaid on the coherence volume, and (d) most-positive curvature (same as Figure 11c) overlaid on the coherence volume. Note that the overlay slice helps to show the corresponding relation between all three attributes when delineating the stratigraphic features.

compacted less than the flood plain and may be sand-filled. If it is tightly correlated with a negative curvature anomaly, it is either incised or has been filled with material that has compacted more than the surrounding flood plain. Note that the curvature shows more subtle

features not observed by coherence because coherence is focused on measuring the lateral discontinuities.

Al-Dossary and Marfurt (2006) use different wavelength curvature attributes to enhance geologic features having different scales. Li and Lu (2014) use

Figure 13. A time slice at $t = 510$ ms through (a) most-negative curvature (long-wavelength) and (b) most-negative curvature (short-wavelength) volumes run on input seismic data, (c) most-negative curvature (long-wavelength), and (d) most-negative curvature (short-wavelength) volumes run on seismic data with enhanced resolution. Note that the points of comparison denoted by green arrows show subtle channels, which cannot be detected by most-positive curvature shown in Figure 11.

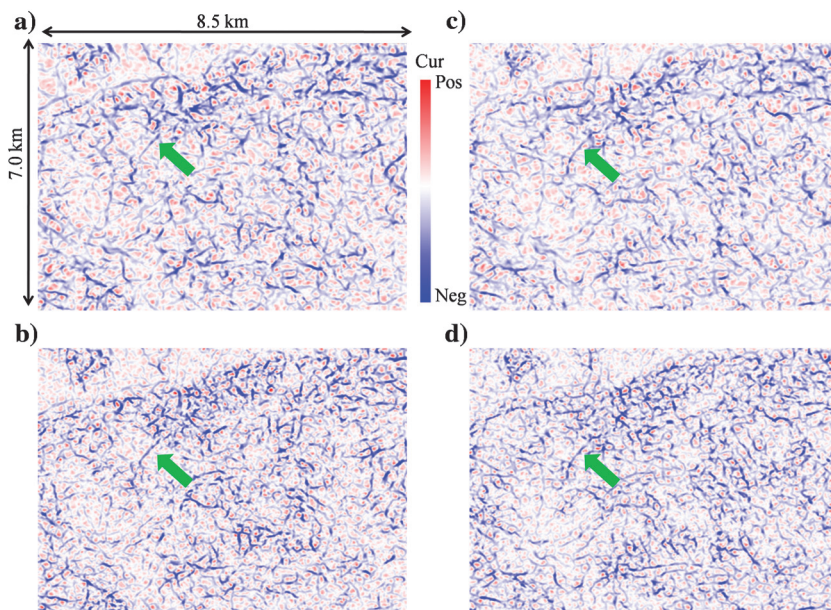


Figure 14. A time slice at $t = 510$ ms through (a) most-positive curvature volume, (b) coherence, (c) most-negative curvature, and (d) most-positive and negative curvature overlaid on coherence.

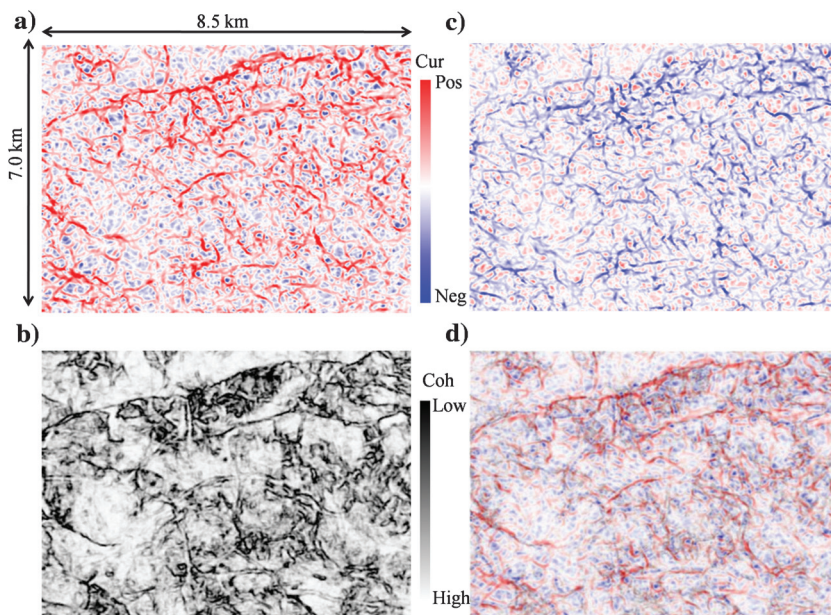
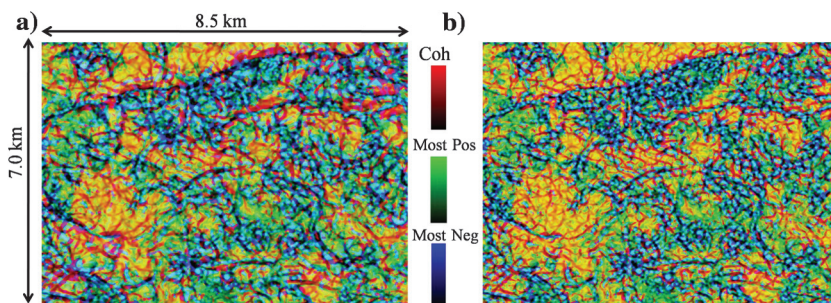


Figure 15. A time slice at $t = 510$ ms through (a) composite volume of long-wavelength most-positive, most-negative curvature, and coherence and (b) composite volume of short-wavelength most-positive, most-negative curvature, and coherence. Note that the composite images show the clear edges of major faults and channels.



color-blended technique to integrate complex spectral coherence attributes at different scales and get promising results. Here, we also use RGB technique to generate the color-blended images. Figure 15a shows an integration attribute slice extracted from the composite volume of coherence, long-wavelength most-positive, and most-negative curvatures, whereas Figure 15b is calculated from coherence, short-wavelength most-positive, and most-negative curvatures. We can find the major trends of faults and channels in Figure 15a and more details in Figure 15b.

Conclusions

Spectral balancing is critical in improving the resolution of thin beds such as the fluvial channels seen in the Bohai Gulf. Time-variant spectral balancing and inverse Q -filtering improve the resolution of the original seismic data, providing a means of more accurate channel mapping. Our proposed NPF spectral-modeling technique provides the best results of the three spectral balancing algorithms, as seen on vertical slices through seismic amplitude and time slices through seismic attributes. Spectral balancing improves some attributes but not others. The most direct impact is on spectral components. The bandwidth is extended, and the mean frequencies are increased, providing a greater dynamic range of the spectral decomposition images. The phase is nearly unchanged. By construction, spectral balancing results in tighter seismic wavelets than the original seismic data. Such tighter wavelets allow the use of a smaller analysis window in our coherence computation and subsequently in the delineation of the edges of thinner channels. Because spectral balancing is applied trace to trace, it should not radically change the appearance of larger folds and flexures. However, individual channels may undergo different amounts of differential compaction. Improving the vertical resolution allows us to map such features as lithology indicators.

Our new spectral modeling algorithm does not address dispersion effects associated with intrinsic attenuation. In theory, inverse Q -filtering should further improve resolution by compensating for such dispersion. We attribute this lack of greater improvement to a strong component of our attenuation due to geometric scattering.

Acknowledgments

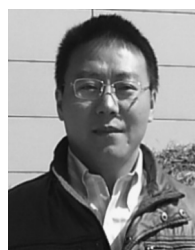
This work is financially supported by the National Natural Science Foundation of China (grant no. 41204091), and the Science and Technology Support Program (grant no. 2011GZ0244) from the Science and Technology Department of Sichuan Province of China. The first author appreciates the Chinese Scholarship Council for financial support. The second author (corresponding author) thanks J. Wang of Chengdu University of Technology for his beneficial suggestion. We thank the Bureau of Geophysical Prospecting of China National Petroleum Corporation for providing field data. We are also grateful to H. Zeng, Y. Sun, and three anonymous reviewers for their constructive sugges-

tions and comments. Coherence and curvature attributes referred to in this paper were calculated using AASPI software from the University of Oklahoma.

References

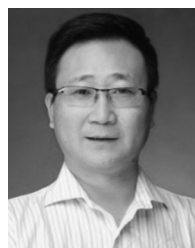
- Al-Dossary, S., and K. J. Marfurt, 2006, 3D volumetric multi-spectral estimates of reflector curvature and rotation: *Geophysics*, **71**, no. 5, P41–P51, doi: [10.1190/1.2242449](https://doi.org/10.1190/1.2242449).
- Barnes, A., 2000, Weighted average seismic attributes: *Geophysics*, **65**, 275–285, doi: [10.1190/1.1444718](https://doi.org/10.1190/1.1444718).
- Chopra, S., 2011, Coherence and curvature attributes on preconditioned seismic data: *The Leading Edge*, **30**, 386–393, doi: [10.1190/1.3575281](https://doi.org/10.1190/1.3575281).
- Chopra, S., A. Alexeev, and V. Sudhakar, 2003, High-frequency restoration of surface seismic data: *The Leading Edge*, **22**, 730–738, doi: [10.1190/1.1605071](https://doi.org/10.1190/1.1605071).
- Chopra, S., J. Castagna, and O. Portniaguine, 2006, Seismic resolution and thin-bed reflectivity inversion: *CSEG Recorder*, **1**, 19–25.
- Chopra, S., and K. J. Marfurt, 2007, Seismic attributes for prospect identification and reservoir characterization: *SEG*.
- Fomel, S., 2007, Shaping regularization in geophysical-estimation problems: *Geophysics*, **72**, no. 2, R29–R36, doi: [10.1190/1.2433716](https://doi.org/10.1190/1.2433716).
- Fomel, S., 2009, Adaptive multiple subtraction using regularized nonstationary regression: *Geophysics*, **74**, no. 1, V25–V33, doi: [10.1190/1.3043447](https://doi.org/10.1190/1.3043447).
- Fomel, S., and Y. Liu, 2010, Seislet transform and seislet frame: *Geophysics*, **75**, no. 3, V25–V38, doi: [10.1190/1.3380591](https://doi.org/10.1190/1.3380591).
- Futterman, W. I., 1962, Dispersive body waves: *Journal of Geophysical Research*, **67**, 5279–5291, doi: [10.1029/JZ067i013p05279](https://doi.org/10.1029/JZ067i013p05279).
- Gabor, D., 1946, Theory of communication. Part 1: The analysis of information: *Journal of the Institution of Electrical Engineers*, **93**, 429–441, doi: [10.1049/ji-3-2.1946.0074](https://doi.org/10.1049/ji-3-2.1946.0074).
- Gao, J. H., W. C. Chen, Y. M. Li, and F. Tian, 2003, Generalized S transform and seismic response analysis of thin interbeds surrounding regions by GPS: *Chinese Journal of Geophysics*, **46**, 759–768, doi: [10.1002/cjg2.3370](https://doi.org/10.1002/cjg2.3370).
- Hale, D., 1982, Q adaptive deconvolution: *Stanford Exploration Project*, **30**, 133–158.
- Hargreaves, N. D., 1992, Similarity and inverse Q filter: Some simple algorithms for inverse Q filtering: *Geophysics*, **57**, 944–947, doi: [10.1190/1.1443307](https://doi.org/10.1190/1.1443307).
- Hargreaves, N. D., and A. J. Calvert, 1991, Inverse Q filtering by Fourier transform: *Geophysics*, **56**, 519–527, doi: [10.1190/1.1443067](https://doi.org/10.1190/1.1443067).
- Huang, N. E., Z. Shen, S. R. Long, M. C. Wu, H. H. Shih, Q. Zheng, N. C. Yen, C. C. Tung, and H. H. Liu, 1998, The empirical mode decomposition and the Hilbert spectrum for nonlinear and non-stationary time series analysis: *Proceedings of the Royal Society of London, Series A: Mathematical, Physical and Engineering Sciences*, **454**, 903–995, doi: [10.1098/rspa.1998.0193](https://doi.org/10.1098/rspa.1998.0193).

- Kjartansson, E., 1979, Constant Q wave propagation and attenuation: *Journal of Geophysical Research*, **84**, 4737–4748, doi: [10.1029/JB084iB09p04737](https://doi.org/10.1029/JB084iB09p04737).
- Leppard, C., A. Eckersley, and S. Purves, 2010, Quantifying the temporal and spatial extent of depositional and structural elements in 3D seismic data using spectral decomposition and multiattribute RGB blending, *in* L. J. Wood, T. T. Simo, and N. C. Rosen, eds., *Seismic imaging of depositional and geomorphic systems*, 30th annual GCSSEPM Foundation Bob F. Perkins Research Conference, GCSSEPM, 1–10.
- Li, F. Y., and W. K. Lu, 2014, Coherence attribute at different spectral scales: *Interpretation*, **2**, no. 1, SA99–SA106, doi: [10.1190/INT-2013-0089.1](https://doi.org/10.1190/INT-2013-0089.1).
- Liu, G. C., S. Fomel, and X. H. Chen, 2011, Time-frequency analysis of seismic data using local attributes: *Geophysics*, **76**, no. 6, P23–P34, doi: [10.1190/geo2010-0185.1](https://doi.org/10.1190/geo2010-0185.1).
- Liu, J., and K. J. Marfurt, 2007, Instantaneous spectral attributes to detect channels: *Geophysics*, **72**, no. 2, P23–P31, doi: [10.1190/1.2428268](https://doi.org/10.1190/1.2428268).
- Marfurt, K. J., and R. L. Kirlin, 2001, Narrow-band spectral analysis and thin-bed tuning: *Geophysics*, **66**, Special section, 1274–1283, doi: [10.1190/1.1487075](https://doi.org/10.1190/1.1487075).
- Marfurt, K. J., and M. Matos, 2014, Am I blue? Finding the right (spectral) balance: *AAPG Explorer*, **35**, 46–47.
- Margrave, G. F., and M. P. Lamoureux, 2001, Gabor deconvolution: *CREWES Research Report*, **13**, 241–276.
- Margrave, G. F., M. P. Lamoureux, and D. C. Henley, 2011, Gabor deconvolution: Estimating reflectivity by nonstationary deconvolution of seismic data: *Geophysics*, **76**, no. 3, W15–W30, doi: [10.1190/1.3560167](https://doi.org/10.1190/1.3560167).
- Matos, M. C., K. J. Marfurt, P. R. S. Johann, J. A. Rosseto, A. T. A. Lourenco, and J. L. Diniz, 2009, Wavelet transform Teager-Kaiser energy applied to carbonate field in Brazil: *The Leading Edge*, **28**, 708–713, doi: [10.1190/1.3148413](https://doi.org/10.1190/1.3148413).
- McFadden, P. D., J. G. Cook, and L. M. Forster, 1999, Decomposition of gear vibration signals by generalized S-transform: *Mechanical Systems and Signal Processing*, **13**, 691–707, doi: [10.1006/mssp.1999.1233](https://doi.org/10.1006/mssp.1999.1233).
- Neep, J. P., 2007, Time variant colored inversion and spectral bluing: 69th Annual International Conference and Exhibition, EAGE, Extended Abstracts, B009.
- Partyka, G., J. Gridley, and J. Lopez, 1999, Interpretational applications of spectral decomposition in reservoir characterization: *The Leading Edge*, **18**, 353–360, doi: [10.1190/1.1438295](https://doi.org/10.1190/1.1438295).
- Pinnegar, C. R., and L. Mansinha, 2003, Time local spectral analysis for non-stationary time series: The S-transform for noisy signals: *Fluctuation and Noise Letters*, **3**, L357–L364, doi: [10.1142/S02194775030001439](https://doi.org/10.1142/S02194775030001439).
- Rioul, O., and M. Vetterli, 1991, Wavelets and signal processing: *IEEE Transactions on Signal Processing*, **8**, 14–38, doi: [10.1109/79.91217](https://doi.org/10.1109/79.91217).
- Rosa, A. L. R., and T. J. Ulrych, 1991, Processing via spectral modeling: *Geophysics*, **56**, 1244–1251, doi: [10.1190/1.1443144](https://doi.org/10.1190/1.1443144).
- Stockwell, R. G., L. Mansinha, and R. P. Lowe, 1996, Localization of the complex spectrum: The S transform: *IEEE Transactions on Signal Processing*, **44**, 998–1001, doi: [10.1109/78.492555](https://doi.org/10.1109/78.492555).
- Taner, M. T., and S. Treitel, 2003, A robust method for Q estimation: 73rd Annual International Meeting, SEG, Expanded Abstracts, 710–713.
- Van der Baan, M., 2008, Time-varying wavelet estimation and deconvolution by kurtosis maximization: *Geophysics*, **73**, no. 2, V11–V18, doi: [10.1190/1.2831936](https://doi.org/10.1190/1.2831936).
- Wang, L. L., J. H. Gao, W. Zhao, and X. D. Jiang, 2013, Enhancing resolution of nonstationary seismic data by molecular-Gabor transform: *Geophysics*, **78**, no. 1, V31–V41, doi: [10.1190/geo2011-0450.1](https://doi.org/10.1190/geo2011-0450.1).
- Wang, Y. H., 2007, Seismic time-frequency spectral decomposition by matching pursuit: *Geophysics*, **72**, no. 1, V13–V20, doi: [10.1190/1.2387109](https://doi.org/10.1190/1.2387109).
- Wang, Y. H., 2010, Multichannel matching pursuit for seismic trace decomposition: *Geophysics*, **75**, no. 4, V61–V66, doi: [10.1190/1.3462015](https://doi.org/10.1190/1.3462015).
- Yilmaz, ö., 2001, *Seismic data processing*, 2nd ed.: vol. 1, SEG.
- Zhang, X. W., L. G. Han, F. J. Zhang, and G. Y. Shan, 2007, An inverse Q -filter algorithm based on stable wavefield continuation: *Applied Geophysics*, **4**, 263–270, doi: [10.1007/s11770-007-0040-9](https://doi.org/10.1007/s11770-007-0040-9).
- Ziolkowski, A., 1991, Why don't we measure seismic signatures?: *Geophysics*, **56**, 190–201, doi: [10.1190/1.1443031](https://doi.org/10.1190/1.1443031).



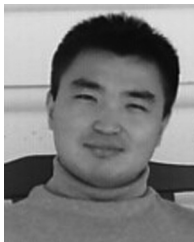
Huailai Zhou received a Ph.D. (2009) in earth exploration and information techniques from the Chengdu University of Technology. He completed his postdoctoral research at the Institute of Sedimentary Geology at the Chengdu University of Technology from 2010 to 2012. He was sponsored by the China Scholarship Council to

work as a part of postdoctoral research faculty in AASPI of the University of Oklahoma, from October 2013 to October 2014. He currently works in the Chengdu University of Technology as an associate professor, and his research work is mainly focused on seismic data processing methods, seismic modeling and imaging, techniques for improving seismic resolution, seismic attributes analysis, and inversion methods.



Yuanjun Wang received a Ph.D. (2007) in geology from the Chengdu University of Technology. He currently serves as a professor of geophysics within the college of geophysics in Chengdu University of Technology, China. His primary research fields include reservoir prediction, mathematical geology, and reservoir sedi-

mentology.



Tengfei Lin received a B.S. (2011) in seismic exploration from the China University of Petroleum (Huadong), and an M.S. (2014) in geophysics from the University of Oklahoma. He currently is a Ph.D. candidate of geophysics at the University of Oklahoma. In the summer of 2011 and 2012, he did two internships at the China National

Petroleum Company in Zhuozhou Hebei and Beijing of China. His research interests include, seismic processing, velocity analysis, attributes analysis of time-depth domain seismic data, and anisotropy analysis.



Fangyu Li received B.S. (2009) and M.S. (2013) degrees in electrical engineering from Beihang University and Tsinghua University. He is pursuing a Ph.D. in geophysics at the University of Oklahoma. His dissertation is about prestack seismic attribute analysis for resources plays.



Kurt J. Marfurt joined the University of Oklahoma (OU) in 2007, where he serves as the Frank and Henrietta Schultz professor of geophysics within the ConocoPhillips School of Geology and Geophysics. His primary research interests include development and calibration of new seismic attributes to aid in seismic processing, seismic interpretation, and reservoir characterization. Recent work has focused on correlating seismic attributes such as volumetric curvature, impedance inversion, and azimuthal anisotropy with image logs and microseismic measurements with a particular focus on resource plays. In addition to his teaching and research duties at OU, he leads short courses on attributes for SEG and AAPG.

work has focused on correlating seismic attributes such as volumetric curvature, impedance inversion, and azimuthal anisotropy with image logs and microseismic measurements with a particular focus on resource plays. In addition to his teaching and research duties at OU, he leads short courses on attributes for SEG and AAPG.